

The rotating wall machine: A device to study ideal and resistive magnetohydrodynamic stability under variable boundary conditions

C. Paz-Soldan, W. F. Bergerson, M. I. Brookhart, D. A. Hannum, R. Kendrick, G. Fiksel, and C. B. Forest

Department of Physics, University of Wisconsin, 1150 University Ave, Madison, Wisconsin 53706, USA

(Received 31 July 2010; accepted 4 October 2010; published online 7 December 2010)

The rotating wall machine, a basic plasma physics experimental facility, has been constructed to study the role of electromagnetic boundary conditions on current-driven ideal and resistive magnetohydrodynamic instabilities, including differentially rotating conducting walls. The device, a screw pinch magnetic geometry with line-tied ends, is described. The plasma is generated by an array of 19 plasma guns that not only produce high density plasmas but can also be independently biased to allow spatial and temporal control of the current profile. The design and mechanical performance of the rotating wall as well as diagnostic capabilities and internal probes are discussed. Measurements from typical quiescent discharges show the plasma to be high β ($\leq p > 2\mu_0/B_z^2$), flowing, and well collimated. Internal probe measurements show that the plasma current profile can be controlled by the plasma gun array. © 2010 American Institute of Physics. [doi:10.1063/1.3505487]

I. INTRODUCTION AND MOTIVATION

Toroidal magnetic confinement devices must either stabilize or avoid long wavelength external kink modes, a class of magnetohydrodynamic (MHD) instability¹ that limits their performance.² In the absence of a conducting wall, instabilities grow on an Alfvénic timescale $\tau_A = L\sqrt{\rho\mu_0}/B$ (L is the spatial scale, ρ is the density, B is the magnetic field) driven by either plasma pressure or current. Though perfectly conducting walls can provide robust stabilization, ohmic losses in resistive walls dissipate the stabilizing eddy currents. On the time scale of this dissipation, $\tau_w = \mu_0\sigma_w r_w \delta_w$ (σ_w is the wall conductivity, r_w is the wall radius, and δ_w is the wall thickness) flux can leak through the wall and allow the perturbation to grow. Instabilities which are stable with perfectly conducting walls but unstable when the walls are resistive are known as resistive wall modes.³

Much theoretical and experimental efforts have concentrated on passive and active stabilization of the resistive wall mode. Progress has been made in reliably controlling tokamak,^{4,5} spherical tokamak (ST),^{6,7} and reversed field pinch (RFP) (Refs. 8 and 9) discharges above the onset criteria for the mode; β ($\leq p > 2\mu_0/B_z^2$) in the tokamak and ST and current in the RFP. This has been achieved through either active magnetic control coils^{7,9} or toroidal rotation imparted by neutral beam heating.^{10,11}

Another proposed method of resistive wall mode stabilization utilizes the rotation of a conducting boundary around the plasma. Theory suggests^{12–15} that if two conducting walls are used and if one wall rotates with respect to the other wall, the mode can be stabilized if both walls are inside the radius for a perfect conductor to stabilize the ideal external kink mode. Inside the moving, resistive wall the magnetic field obeys the magnetic induction equation

$$\frac{\partial \vec{B}}{\partial t} = \nabla \times \vec{V} \times \vec{B} + \frac{1}{\sigma_w \mu_0} \nabla^2 \vec{B}. \quad (1)$$

Here \vec{V} is the wall velocity, where $\vec{V} = \omega_w r_w \hat{\theta}$ (ω_w is the wall angular velocity). If \vec{V} is large enough, the second term dominates the third and the magnetic field perturbation caused by the mode is advected instead of diffused. This slows the leakage of flux and acts to stabilize the mode. As ω_w is increased the growth rate of the resistive wall mode is predicted to decrease, as shown in Fig. 1. Here $R_m = \omega_w \tau_w$ is the wall magnetic Reynolds number, which is defined as the ratio of the second and third terms in Eq. (1). In the moving frame of the wall, any field perturbations appear oscillatory and thus have an electrical skin depth on the order of δ_w . $R_m > 1$ is a required condition for this physical effect to be observed, requiring the very fast rotation rates also shown in Fig. 1. The prototypical instability is a line-tied, external, current-driven kink mode. Following Kruskal and Schwarzschild,¹⁶ Shafranov,¹⁷ and later theory,¹² this mode becomes unstable at $q_a < 1$, where q_a is the edge safety factor ($q_a = 4\pi^2 a^2 B_z / \mu_0 I_p(a) L$, where $I_p(a)$ is the current within radius a , B_z is the axial guide field, and L is the length of the machine) which parameterizes the pitch of the magnetic field lines at the edge of the plasma, where smaller q_a (higher current) is more unstable.

A device has been constructed at the University of Wisconsin-Madison to verify this prediction. The rotating wall machine (RWM), shown in Fig. 2, has the ability to excite ideal and resistive wall modes reproducibly and has been topologically designed to allow for a solid, rotating conducting boundary. The device has a screw pinch magnetic geometry with line-tying provided by thick conducting plates at the anode and by discreteness of the plasma source at the cathode. The characteristic τ_w of the conducting plates is 200 ms, far longer than the discharge duration. Line-tying provides an important point of comparison to the more commonly studied periodic geometry of the torus and is also physically relevant to coronal loops on the surface of the sun.¹⁸ In addition to resistive wall mode stabilization, a focus of research on the device is to determine the nature of the various MHD

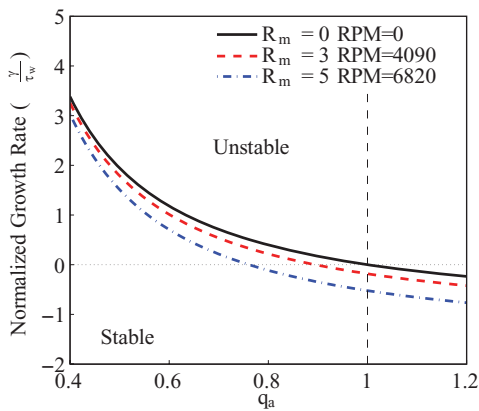


FIG. 1. (Color online) Expected growth rates of the resistive wall mode for a system with $\tau_w = 7$ ms, from analytic theory (Ref. 12). As the wall rotation is increased, the growth rate of the mode is decreased until stabilization occurs. R_m here is the magnetic Reynolds number and q_a is the safety factor at the edge of the plasma.

instabilities seen in the device and to contrast them to the familiar periodic cylinder case.

Previous publications from the RWM have summarized key experimental results under a no-wall boundary condition¹⁹ as well as under conducting and ferritic boundaries.²⁰ Previous work also determined that internal and external current-driven kinks are excited in the RWM. However, no complete description of the device and its plasma characteristics is presently available in the literature. The purpose of this paper is to fill this gap as well as to introduce the design of the rotating wall itself. Discussion of the physics results of the RWM is beyond the scope of this paper.

The organization of this paper is as follows. Section II describes the design and operation of the RWM and associated subsystems such as vacuum maintenance, external magnets, plasma generation, and the rotating wall. Section III discusses

diagnostic systems employed on the device. Typical plasma parameter profiles and plasma controllability are explored in Sec. IV. General discussion of observed plasma parameters and future work is discussed in Sec. V.

II. MACHINE DESCRIPTION

The RWM experimental volume in which the plasma is formed is bounded by a 1.2 m long and 18 cm diameter cylinder, as shown in Fig. 2. The cylinder itself is interchangeable and experiments have been performed with Pyrex[®] (Ref. 19) and various combinations of stainless steel, copper, and mumetal[™].²⁰ The rotating wall assembly is mechanically fixed to the device and is outside the vacuum vessel. It is important to note that there are two resistive walls, the inner static vacuum vessel and the outer rotating wall. At each end are large bell-shaped enclosures that house solenoid magnets, vacuum pumps, diagnostics, and the plasma source array. Including these bells the experiment is 3.3 m long and 1.5 m wide and sits on a rigid stainless steel support structure.

Vacuum is established and maintained at a base pressure of ≈ 0.1 μ Torr using two Welch DuoSeal roughing pumps in conjunction with a Leybold turbomolecular pump with a capacity of 1100 liters/s. The end bell sections are much larger than the diameter of the plasma column to allow for the expansion and escape of unionized neutral gas particles, thus minimizing neutral gas buildup during the discharge.

A. Interchangeable resistive and conducting vacuum walls

To study the effect of different boundary conditions on MHD activity, the experiment has been designed to facilitate the exchange of the cylindrical vacuum vessel wall and liner with relative ease. Commercially available inflatable bladders,

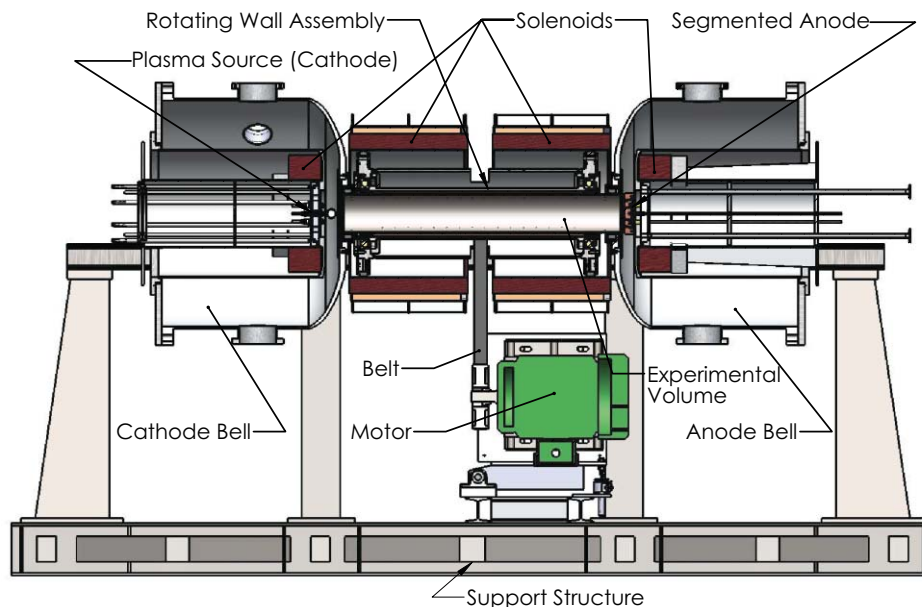


FIG. 2. (Color online) Cross section of the rotating wall machine (RWM): the plasma is generated at the plasma source array and is confined by four solenoids. Biasing the source with respect to the anode drives current throughout the discharge and drives instabilities. The rotating wall and drive motor are also shown.

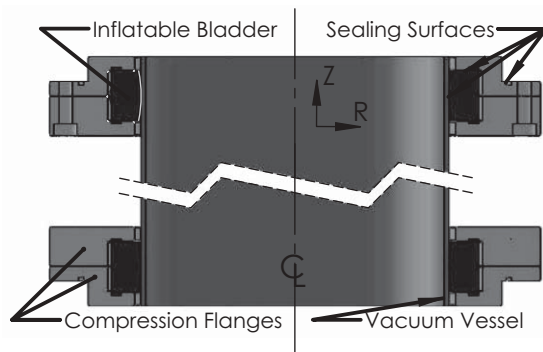


FIG. 3. Cross section of inflatable bladder seal assembly, with sealing surfaces shown. Overlap regions in the drawing indicate compression of the flexible inflatable bladder, both by the flange and by the vacuum vessel. The expansion of the bladder allows a range of vacuum vessel sizes to be accommodated.

shown in Fig. 3, are used for both mechanical support and vacuum sealing. The bladders are compressed by a pair of large flanges and expanded by pressurized air at approximately 60 psi, forming two sealing surfaces. This expansion offers the added benefit of allowing the system to accommodate inner walls which vary in outer diameter by ± 1 cm. Several unique walls have been used on the RWM, as listed in Table I.

B. Magnetic geometry

The RWM employs a screw pinch magnetic geometry, with an externally imposed axial guide field twisted by azimuthal fields generated by the plasma current. The guide field is provided by four discrete solenoids, shown in Fig. 2. Solenoid power is provided by steady-state silicon controlled rectifier (SCR) fired dc supplies capable of generating a 1 kG field on-axis. In a typical discharge, the solenoids are energized several seconds before the plasma source becomes active, yielding a temporal decoupling of the magnetic fluxes arising from the plasma and from the external solenoids. Multiple power supplies yield independent control of the end and central solenoids, allowing variable mirror ratios to be achieved. The solenoids cover a large majority of the experimental volume, dramatically limiting the field ripple. Nonetheless, ripple of about 3.6% is experienced on-axis at the midplane gap and at the end gaps.

TABLE I. Table of wall parameters used on the RWM. The first two are vacuum vessels, the next two are liners wrapped around the 304SS, and only the final wall is capable of rotation.

Description/ material	Thickness δ_w (mm)	Wall time τ_w (ms)	Relative permeability (μ_r)
Pyrex	5	≈ 0	1
304SS	3	0.5	≈ 1
Static copper	0.5	4	1
MuMetal TM	0.2	0.006	1200
Moving copper	0.7	7	1

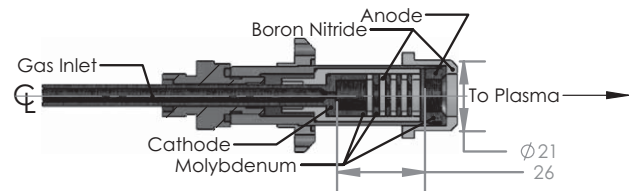


FIG. 4. Cross section of plasma gun: gas is first puffed through the inlet, then a bias is established between the cathode and anode, yielding a high density arc plasma. Alternating boron nitride and molybdenum washers provide stability to the discharge. Dimensions are in millimeters.

C. Plasma generation and current control

The RWM employs an array of 19 high current, high density plasma sources (guns) developed for helicity injection on the Madison Symmetric Torus.^{21,22} Each gun utilizes an alternating arrangement of molybdenum and boron nitride washers, shown in Fig. 4. The effective circuit of each source is shown in Fig. 5 and typical gun traces are shown in Fig. 6. The discharge begins by puffing gas into the plasma gun nozzle. The working gas is either hydrogen or helium. After 2 ms, the gun power supply pulse forming network (PFN) is discharged (box 1 in Fig. 5), thus establishing a high density plasma within the plasma gun nozzle.²¹ This discharge is maintained at 1.2 kA across 100 V for 20 ms by the PFN, as shown in the V_{arc} and I_{arc} traces of Fig. 6. Such large currents

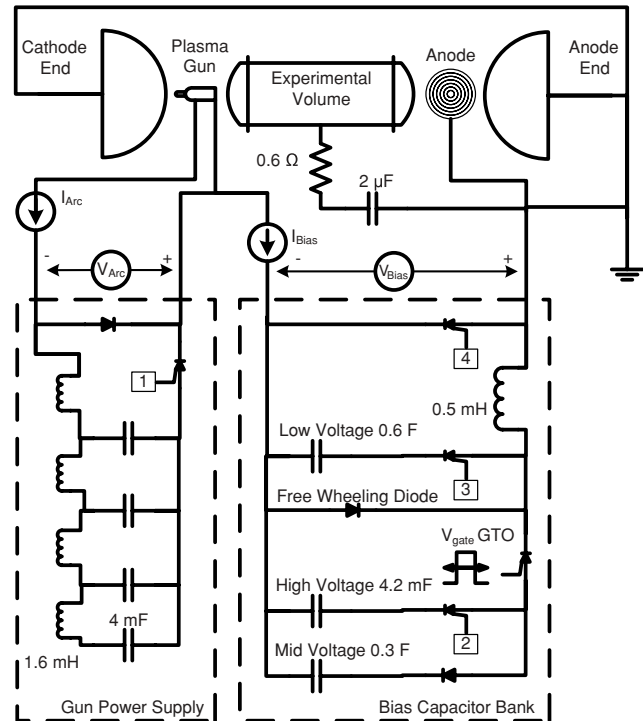


FIG. 5. Illustration of the RWM plasma generation circuit for each plasma source. The gun power supply's pulse forming network (PFN) is first discharged to create a high density plasma in the gun nozzle. High voltage banks then bias the gun relative to the external anode, striking the discharge and quickly bringing the current to the desired level and are then disengaged. The gate turn-off (GTO) thyristor timing circuit decides whether the low or mid voltage banks are active and thus controls the current. Boxes 1–4 are described in Sec. II C.

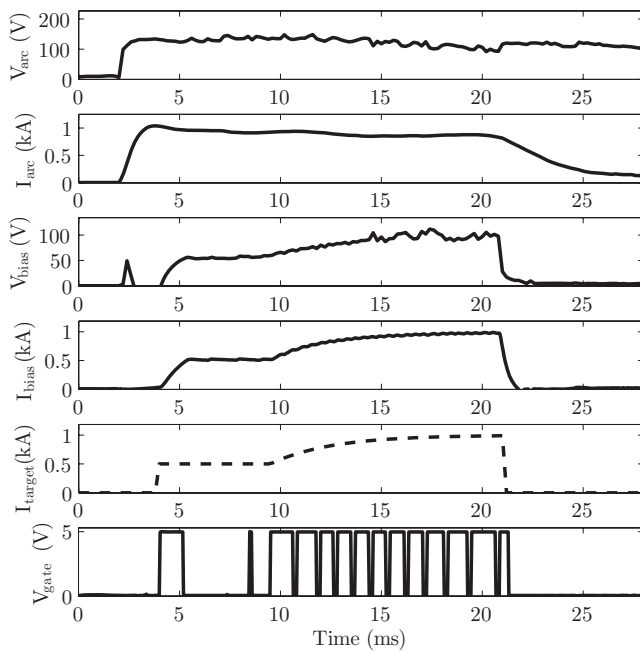


FIG. 6. Typical plasma source time traces, illustrating source operation. The V_{gate} signal controls a GTO, yielding in this case a flat top followed by a slowly ramping current. I_{target} is the desired current waveform, while other measurements correspond to that shown in Fig. 5.

are possible due to the very high density plasma formed inside the gun nozzle which allows for large space-charge limited emission.

The next stage in the discharge begins when the gun is biased relative to the anode of the machine. The bias voltage is established by independent capacitor banks, shown in Fig. 5. After 1 ms, a high voltage capacitor bank is discharged (box 2 in Fig. 5) to negatively bias the source with respect to the anode and quickly ramp the current. After 2 ms, a low voltage capacitor bank is enabled to continually supply the plasma current (box 3 in Fig. 5). Additionally, a feedback system based on pulse width modulation begins to control the bias current (I_{bias} in Figs. 5 and 6) by switching on or off a mid voltage capacitor bank. A control signal (V_{gate} in Figs. 5 and 6) is determined by a comparator circuit which makes a decision based on the reference and actual I_{bias} waveform. If the measured current is above (below) the requested current waveform, the mid voltage capacitors will be disengaged (engaged), thus dropping (raising) the current. This system controls I_{bias} for the duration of the discharge, and after 20 ms a shorting SCR is triggered (box 4 in Fig. 5) which terminates the discharge. Due to cooling requirements the guns operate at a low duty cycle with discharges taking place every 3 min.

The feedback system described is unique to each plasma source, thus allowing per-gun control of injected current. The RWM employs an array of plasma sources, which are arranged in a hexagonal array as shown in Fig. 7, to generate current profiles that can be controlled in both space and time. This regulation not only provides for controllable and repeatable current waveforms but also assures balanced current injection from each gun. Switching is achieved on the microsecond time scale through the use of gate turn-off (GTO) thyristors. The use of the current controller is illustrated in

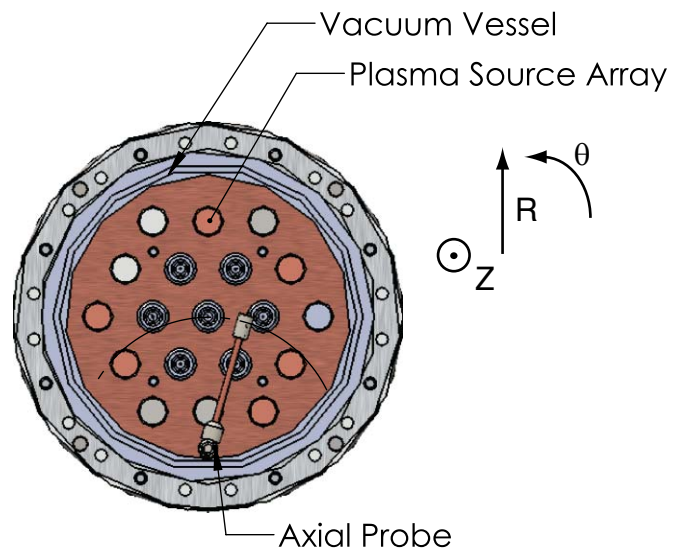


FIG. 7. (Color online) A face-on view of the plasma source (gun) array. There are 19 guns in the array, though only the central seven are usually used. Varying the amount of current injected per gun allows spatial and temporal controls of the current profile. The geometry of the internal probe is also shown in this view along with the trajectory it sweeps.

Fig. 6, where the V_{gate} signal controls the capacitor bank and produces a ramped current profile.

D. Rotating wall

As discussed in Sec. I, the RWM rotating wall must be able to achieve $R_m > 1$ to influence the stability of the resistive wall mode. The wall has been designed to reach $R_m \approx 5$ which necessitates rotation rates in excess of 6500 rpm or 240 km/h ($\omega_w \approx 700$ rad/s), using a design τ_w of 7 ms.

The rotating wall is a precision-engineered product. A cross section schematic of the assembly is shown in Fig. 8 and installed in the RWM in Fig. 2. The rotating shaft has an outer diameter of 20 cm and is 1 m long and 1 cm thick. It is made of 304SS with a 1 mm thick copper liner on the inner diameter which was installed via a thermal interference fit. The copper provides electrical conductivity to increase τ_w , while the 304SS provides mechanical strength. The shaft is held by two SKF 71940 hybrid angular contact ball bearings compressed against each other by Belleville spring loaded flanges, thus ensuring axial rigidity and radial load bearing capability. The balls are made of silicon nitride, which allows greater maximum speeds and electrically isolates the shaft from the RWM, thus preventing unwanted induced currents during the plasma discharge. The bearings are housed in a self-contained cassette that provides both mechanical strength and modularity to the design. The assembly is mechanically coupled to the inner diameter of the central solenoids of the RWM by inflatable bladders in a process similar to that of Sec. II A. Mechanical power is provided by a Reliance P25G4900 11 kW three phase electric motor controlled by a Danfoss variable frequency drive. A flat belt couples power from the motor to the shaft, as shown in Fig. 2. The motor is housed in a custom frame that allows fine tuning of motor yaw to maintain belt position. Bearing lubrication is provided by an

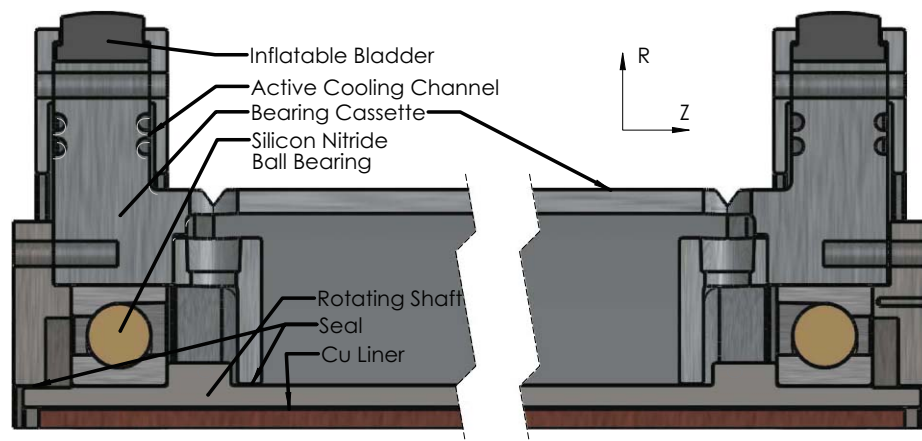


FIG. 8. (Color online) Cross sectional view of rotating wall assembly. The shaft is held in place by angular contact bearings and can rotate at a maximum speed of 280 km/h.

SKF OLA05 oil-spot unit. Compressed air delivers a steady stream of Mobil Velocite spindle oil to the bearings and provides active cooling.

The rotating wall can achieve maximum speeds of 7500 rpm, or 280 km/h, though maximum normal operation is closer to 6500 rpm, or 240 km/h. Speed is measured by an encoder on the motor and an optical tachometer on the shaft. During normal operation the bearings operate near 40°C, as measured by eight thermocouples on the end flanges which are also capable of localized measurements of any thermal excursions. Power measurements to the motor show that approximately 3 kW are required to drive the motor to the nominal maximum operating speed, of which 1 kW is used internally within the motor. Nominal vibration amplitudes are 5 mm/s. on the motor and 1 mm/s. on the shaft. Vibration does increase above 250 km/h as shaft imbalances begin to dominate.

III. PLASMA DIAGNOSTICS

A defining feature of the RWM geometry is the inaccessibility of the experimental volume from the radial direction due to the topological constraint of the rotating wall. Thus, all diagnostics and feedthroughs must enter from either end of the machine.

A. Current profile and segmented anode

The linear nature of the RWM allows for spatial and temporal accounting of the currents in the machine. Utilizing shunt resistors on the plasma source and bias capacitors (I_{arc} and I_{bias} in Fig. 5) the amount of current entering the machine is well known. Currents to the end bells and central tube of the machine are measured by Rogowski coils. The anode of the machine comprises a thick copper disk surrounded by two thick concentric rings, shown in Fig. 9. Rogowski coils are also placed on the leads exiting each anode segment, allowing all currents leaving the machine to be measured. The segmented anode thus provides a coarse current profile within the machine which can be related to the safety factor profile, the critical parameter in current-driven MHD stability studies.²³

B. Magnetic field measurements

For the study of MHD stability and to characterize MHD modes, arrays of fluxloops and coils are used. The RWM employs 30 B_θ coils, 10 B_z coils, and 80 B_r fluxloops at the edge of the experimental volume in a geometry shown in Fig. 10. Each signal is integrated by Sterling Scientific analog integrators prior to being simultaneously digitized at 0.5–1 MHz, allowing full resolution of all dynamics in the device. Simultaneous digitization also allows spatial Fourier decomposition of the azimuthal mode spectrum. Fourier decomposition in the z -direction is not amenable since two axial wavenumbers are required to satisfy the line-tied boundary conditions. Three fluxloops encircling the entire plasma cross section are also in place to measure the volume averaged diamagnetism.

C. Axial probes and 2D drive mechanism

The RWM plasma is well suited to internal probe work as the heat fluxes are tolerable and the discharges are highly reproducible. To access the vessel an axial probe drive mechanism is used that allows probe insertion from the anode of the machine. Due to geometric constraints of the probe feedthrough, inserted probes must have a diameter of no greater than 13 mm. A 90° articulating joint has been developed that allows the probe to swing into the radial direction

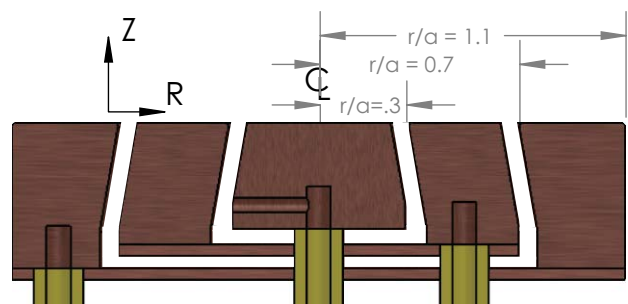


FIG. 9. (Color online) Cross section of the copper segmented anode, illustrating both the support scheme as well as the complete coverage of the target. The thickness of this section (5 cm), along with the highly conductive material used, maintains the line-tied condition at the anode.

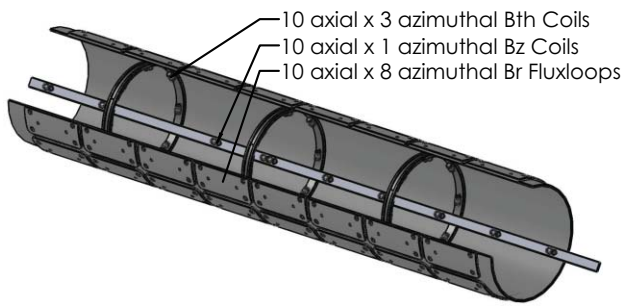


FIG. 10. Drawing illustrating location of the magnetic diagnostics on the RWM. There are 30 B_θ coils, 10 B_z coils, and 80 B_r fluxloops which together provide complete coverage of the experimental volume.

once it has passed the feedthrough and entered the experimental volume. It is shown in Fig. 11. Using stepper motors, the articulated probe is able to sweep an arc in the (r, θ) plane, shown in Fig. 7. Assuming azimuthal symmetry, probe mobility in the axial (z) direction allows (r, z) contour maps of the plasma to be generated. This technique relies on the established shot-to-shot repeatability of the discharge when dealing with slow (≤ 1 kHz) dynamics.

Several probe heads utilize the same insertion and control system. A single-tip Langmuir probe is extensively used to characterize electron temperature, density, and plasma potential through I - V curve characterization. The Langmuir probe utilizes a tungsten wire of 0.4 mm diameter that is insulated from the plasma by a quartz stalk of 4 mm diameter that is filled with boron nitride powder. In addition, a three-axis magnetic fluctuation (B-dot) probe has been designed and deployed, shown in Fig. 12. The probe is constructed with a thermally fit stainless steel mechanical structure which also serves as an electrostatic shield, with boron nitride insulating the coil region and quartz insulating the stalk. The steel structure limits the high-frequency response of the probe to 100 kHz. Plasma parameters measured by these probes will be discussed in Sec. IV. A two-tip Mach probe is also used on the RWM to measure \hat{z} -directed flows. It is constructed by tightly fitting a 4 mm diameter quartz tube over a quartz rod with channels ground out for the 0.4 mm wire, which extends

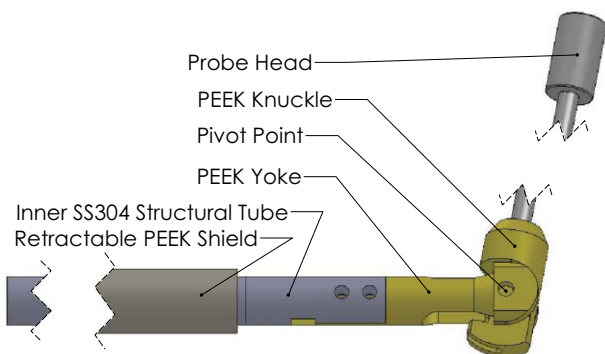


FIG. 11. (Color online) Drawing illustrating the articulating knuckle used to position radial armature of probe after insertion through a 13 mm tube. The retractable polyether ether ketone (PEEK) thermoplastic shield slides flush with the semicircular section, locking the joint into a right angle. This is done *in situ* with a custom rod tool through a vacuum window.

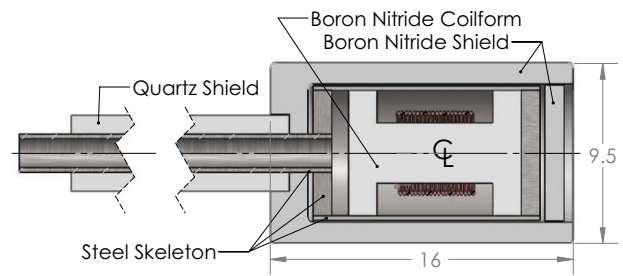


FIG. 12. (Color online) Magnetic probe cross section, illustrating the thermally fit, interlocking SS316 skeleton providing rigidity and electrostatic shielding as well as the boron nitride and quartz plasma shielding. Dimensions are in millimeters.

slightly above the tube. The rod extends beyond the wires to provide insulation between the tips.

IV. OBSERVED PLASMA PARAMETERS AND PROFILE CONTROL

The central parameters varied during experiments on the RWM are the axial guide field (B_z) and plasma current density profile [$J_z(r, t)$], with the resulting discharges being highly reproducible on a slow-time scale ($\tau \geq 1$ ms). This indicates that similar global MHD equilibria are achieved for similar input parameters. Some equilibria are prone to ideal¹⁹ or resistive²⁰ MHD instabilities, while others are stable and quiescent. To give a flavor of the plasmas produced by the RWM, measured plasma parameter profiles for different hydrogen gas equilibria are described in this section. Measurements are taken by the probes described in Sec. III C, with each spatial location corresponding to a single discharge. Plasma reproducibility allows both radial and axial profiles to be assembled with a standard grid spacing of 5 mm radially and 10 cm axially.

A. Kinetic profiles

Kinetic profiles (n_e, T_e) generated by the plasma source array are characterized by a monotonically increasing in radius and very high density ($n_e \approx 1\text{--}5 \times 10^{14}$ cm⁻³) coupled with a cold and essentially uniform electron temperature ($T_e \approx 3.5$ eV). As T_e is constant, only profiles of n_e are shown in Fig. 13. The 0 kA case corresponds to the gun power supply circuit (shown in Fig. 5) discharging but with the bias capacitor bank disconnected. This configuration yields a low density, noncurrent-carrying plasma. As the plasma guns are biased to drive current, a dramatic increase in the plasma density is seen. The large amount of ohmic heating power ($\approx 0.2\text{--}0.6$ MW) from the bias capacitor bank is thus primarily ionizing new plasma particles. The electron temperature is relatively constant at 3–4 eV as gun current is increased likely due to the fact that the poor axial confinement precludes the electrons from gaining much energy before they are lost to the ends. The plasma pressure can also be calculated, assuming quasineutrality and cold ions, as a product

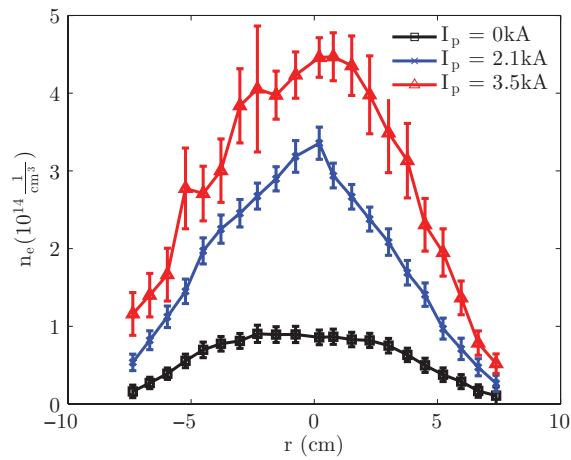


FIG. 13. (Color online) Plasma density profiles from single-tip Langmuir probe for different injected gun currents. Increased gun injection current (ohmic heating) strongly increases the plasma density, while T_e remains relatively constant (not shown).

of these two values, yielding a volume averaged value of β approaching 10%.

B. Current profiles

The magnetic probe described in Sec. III C is used to measure the equilibrium currents and magnetic fields in the RWM plasma. Using the differential form of Ampere's law ($\nabla \times \vec{B} = \mu_0 \vec{J}$), the radial profile of B_θ can be related to the axial current profile, assuming azimuthal axisymmetry. The current density profile shown in Fig. 14 is created with the central seven guns each producing an equal amount of current, yet the profile is strongly peaked as opposed to the top-hat shape assumed in theory.¹² As a check of the probe measurement, the coarse current profile measured by the segmented anode is also shown in Fig. 14, illustrating good agreement between the two methods.

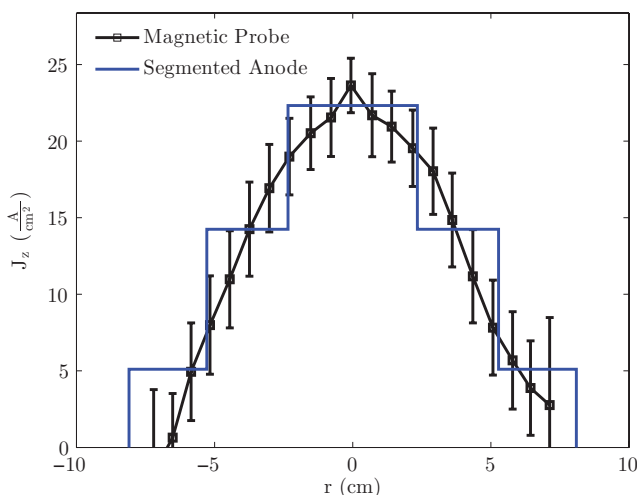


FIG. 14. (Color online) Axial current profile from internal magnetic probes utilizing ensemble averaging, illustrating a single collimated current channel. The discrete current filaments from the plasma source array have merged by this point in the discharge ($Z = 89 \text{ cm}$). The current measured by the segmented anode is also plotted and shows good agreement.

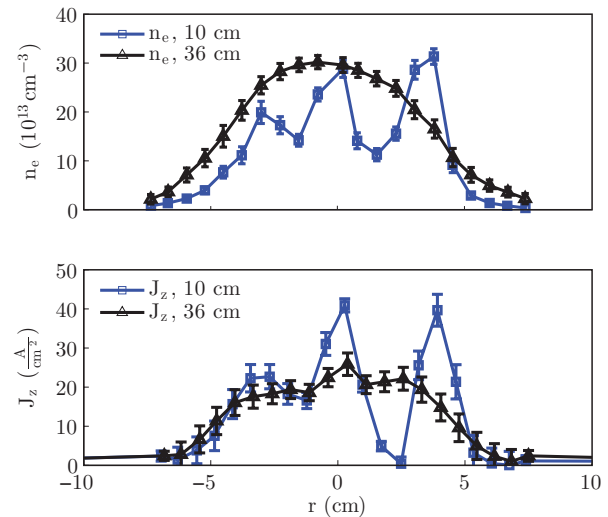


FIG. 15. (Color online) Relative radial profiles of both n_e (above) and J_z (below) both near to (10 cm) and farther from (36 cm) the plasma gun array. The discrete flux ropes exiting the gun are seen to merge (in both current and density) within 36 cm from the gun.

1. Discrete source merging

The plasma source array injects current-carrying plasma into the experimental volume at discrete locations which then merge. Internal probe measurements are able to measure the merger of the discrete flux ropes, with both kinetic (n_e) and current profiles shown in Fig. 15. Profiles near the gun ($Z = 10 \text{ cm}$) illustrate the discretized structures corresponding to the central gun and the inner ring of guns. However, by $Z = 36 \text{ cm}$, these structures are no longer present in both the density and the current profiles, indicating a merger of the flux ropes. The merger in the azimuthal direction is likely accomplished by phase mixing brought on by magnetic shear. Field lines on the center of a single flux rope map to different azimuthal locations than field lines on the edge of the flux rope, thus blending the flux rope into its azimuthal neighbor as it leaves the gun nozzle. The fact that the flux ropes have fully merged within $Z = 36 \text{ cm}$ confirms that parameter profiles are adequately captured by a 1D model.

2. Current profile control

The current injected from each gun in the array can be controlled independently, giving a large degree of control over the current profile in the RWM. As an illustration of spatial control, Fig. 16 illustrates two different current profiles. The first is from a discharge created with the central seven guns of the 19 gun array injecting current. This profile displays a peaked current density and a safety factor minimum on-axis. The other profile shown in Fig. 16 pertains to a discharge in which the central gun was not discharged, leading to a hollow current profile and a correspondingly reverse-shear safety factor ($\partial q / \partial r < 0$) profile with a minimum off-axis. The peaked current profiles are well suited to excited internal kink modes, while the hollow profiles are better suited to external kink mode study.

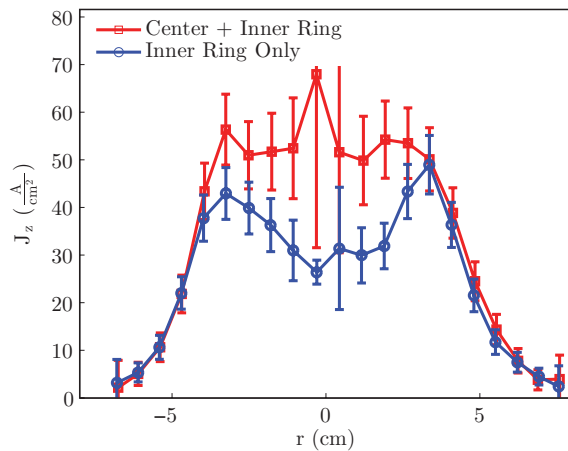


FIG. 16. (Color online) Current profile variation as measured by the internal magnetic probe described in Sec. III C. The case with all seven inner guns injecting current leads to a peaked current profile. When the central gun does not inject current, the profile is hollow. The measurement is taken at $Z = 36$ cm.

The independent gun control also allows temporal control of the current profile. This is shown in Fig. 17, which illustrates current profiles at two distinct times during a discharge in which the central gun current was slowly increased from 500 to 1000 A (as per Fig. 6) while the inner six guns were maintained at a constant current of 500 A each. The increased current injection is clearly visible as an increased central current density. Profiles at other axial locations (not shown) allow studies of perpendicular current transport to be performed. Injected current from all guns can also be increased in tandem, allowing a more gradual transition through the critical current for MHD mode excitation.

C. Electrostatic fields and azimuthal flow

Large radial electric fields have been measured in the RWM plasma. A consequence of the large currents being

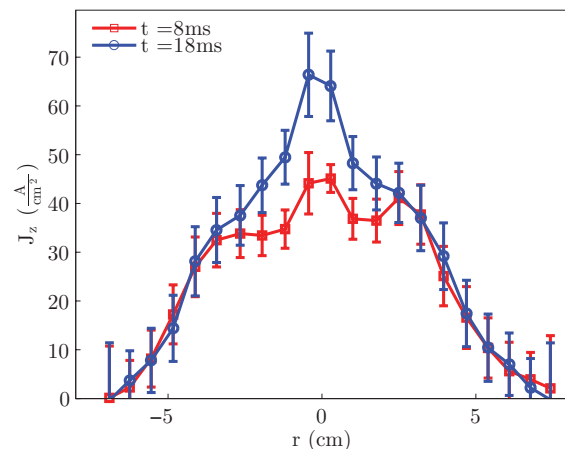


FIG. 17. (Color online) Current profile variation as central gun current is slowly increased from 500 to 1000 A while inner ring delivers a constant 500 A/gun. This illustrates the RWM experimental capability of dynamic per-gun current profile control. This current profile is seen to become very peaked near the gun (where profile is taken) but diffuses outward toward the anode (not shown).

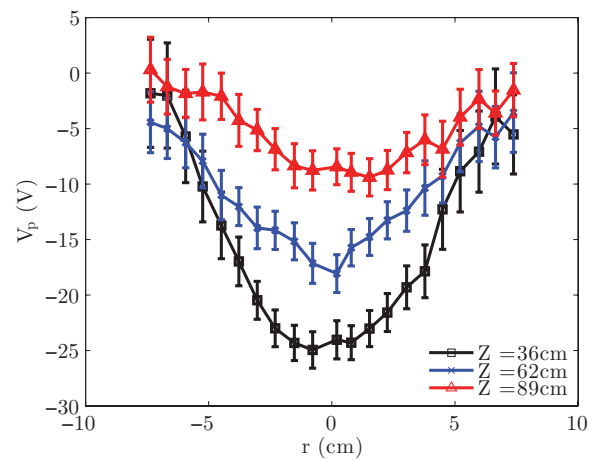


FIG. 18. (Color online) Plasma potential profiles as measured by single tip sweeping Langmuir probe. The radial electric fields shown likely give rise to $\vec{E} \times \vec{B}$ flows which are sheared in both the radial and axial directions.

driven in the cold, resistive RWM plasma is a large potential difference between the anode and cathode, approximately 30 V for this case. This voltage is applied locally at the plasma source array at one end of the experimental volume, while the vacuum vessel wall and anode are near ground. This by necessity creates a radial plasma potential well, shown in Fig. 18, which can drive $\vec{E} \times \vec{B}$ flows in the azimuthal direction. The $\vec{E} \times \vec{B}$ flow also introduces a centrifugal term into the radial force balance, though the relative importance of this term is found to be small. The flows are sheared in both r and z , leading to an ongoing investigation of their effect on MHD stability and other plasma characteristics.

V. DISCUSSION

Probe measurements allow various plasma parameters and dimensionless numbers to be calculated, as shown in Table II. Due to the cold and dense nature of the plasma, the sound speed and the Alfvén speed are comparable. The parallel Lundquist number, a ratio of the Alfvén crossing time to the resistive diffusion time, is relatively low. The plasma β is large, posing the question of whether or not β driven MHD modes can be observed in the device. This is as yet unresolved experimentally or theoretically in the line-tied geometry. The observed plasma parameters indicate that the ideal MHD theory¹² used to predict that resistive wall mode behavior could be significantly improved with the addition of pressure and resistivity. As there is no confinement in the axial direction, the plasma confinement time τ_E is measured to be 10 μ s, similar to the sound transit time across the device length.

The RWM is an ideal device for the study of both resistive and ideal current-driven MHD instabilities in the line-tied geometry. The discreteness of the plasma sources along with a sophisticated current control scheme allows current distributions to be programmed in both space and time, which gives a good degree of control and reproducibility in the excitation of MHD instabilities. For example, disengaging the central plasma source of the array tends to produce reverse-shear

TABLE II. Table of plasma parameters for a typical RWM discharge (specifically the 2.1 kA constant-current discharge described in Sec. IV utilizing the center and inner ring plasma guns).^a

Parameter	Formula	Symbol	Value
Axial field		B_z	500 G
Plasma current		I_p	2.1 kA
Electron density		n_e	$5 \times 10^{14} \text{ cm}^{-3}$
Electron temperature		T_e	3.5 eV
Spitzer resistivity	$10^{-4} \ln(\Lambda) T_e^{-3/2}$	η	230 $\mu\Omega\text{m}$
Electron thermal speed	$(2k_b T_e / m_e)^{1/2}$	v_{Te}	110 km/s
Sound speed	$(\gamma k_b T_e / m_i)^{1/2}$	C_s	24 km/s
Alfven speed	$B_z / (n_i m_i \mu_0)^{1/2}$	v_A	49 km/s
Mach number	v_z / C_s	M	0.3
Alfven time	r / v_A	τ_A	2 μs
Resistive diffusion time	$r^2 \mu_0 / \eta$	τ_{res}	52 μs
Energy confinement time	P_{ohm} / W	τ_E	10 μs
Lundquist number	τ_{res} / τ_A	S	26
Plasma Beta	$2\mu_0 \langle p \rangle / B^2$	β	10 %
Volumetric ohmic heating	$\int \eta J^2 dV$	P_{ohm}	200 kW
Ion mean free path	$(n_i \sigma_i)^{-1}$	λ_i	3 μm
Electron mean free path	$(n_e \sigma_e)^{-1}$	λ_e	500 μm
Ion skin depth	c / ω_{ci}	δ_i	13 mm
Electron skin depth	c / ω_{ce}	δ_e	0.3 mm
Electron larmor radius	v_{Te} / ω_{ce}	ρ_e	0.1 mm

^a $L = 1.22$ m is the plasma length, $r \approx 10$ cm is the plasma diameter. k_b is Boltzmann's constant, γ is the adiabatic index, and Λ is the coulomb logarithm.

safety factor profiles which reduce internal mode activity but maintain external mode activity. Temporal control allows additional current to be injected after an equilibrium has formed in order to investigate current transport. Furthermore, slowly ramping the plasma current allows a more gradual transition through the instability threshold. Active control also assures the reproducibility of the discharge so that individual probe measurements taken at multiple locations over hundreds of discharges can be combined to form a cohesive picture of a single equilibrium.

A. Conclusion and future work

The motivation for constructing the RWM is to test the hypothesis that moving conductors can stabilize the resistive wall mode. The rotating wall described in Sec. D will soon be installed and experiments will attempt to stabilize the resistive wall mode. Depending on the physical results of the solid conductor study, a proposed further effort is to utilize flowing liquid sodium, leveraging the assets of the Madison dynamo facility.²⁴ Flowing liquid metals are topologically suitable to extrapolation to toroidal devices, and positive results could influence future tritium breeder blanket designs in magnetic confinement devices. Future work is also planned in the area of optical spectroscopy. An ion Doppler spectrometry probe²⁵ will be used in conjunction with a 1.5 m focal length Czerny-Turner spectrometer. It is predicted that at the temperatures and densities measured, Stark broadening should dominate the line emission shape and thus provide an independent confirmation of the electron density. Other future work will concentrate on the fundamental plasma physics

of magnetic reconnection,²⁶ with multidimensional fluxloop arrays currently in the design stages. These arrays will be able to simultaneously measure the eigenfunction of the discharge in the 2D (r, θ) plane and attempt to answer questions pertaining to flux rope merging and reconnection.^{27,28}

ACKNOWLEDGMENTS

This work is supported by Department of Energy Grant No. DE-FG02-00ER54603 and National Science Foundation Grant No. 0903900. We wish to thank J. S. Sarff, C. C. Hegna, M. Clark, J. Wallace, and W. Zimmerman for the attention they have given to the project. We also wish to acknowledge the several other individuals from the University of Wisconsin Plasma Physics Group who have provided their time, guidance, and support.

- ¹J. P. Freidberg, *Rev. Mod. Phys.* **54**, 801 (1982).
- ²F. Troyon, R. Gruber, H. Saurenmann, S. Semenzato, and S. Succi, *Plasma Phys. Controlled Fusion* **26**, 209 (1984).
- ³J. Goedbloed, *Nucl. Fusion* **12**, 649 (1972).
- ⁴M. Okabayashi, I. N. Bogatu, M. S. Chance, M. S. Chu, A. M. Garofalo, Y. In, G. L. Jackson, R. J. La Haye, M. J. Lanctot, J. Manickam, L. Marrelli, P. Martin, G. A. Navratil, H. Reimerdes, E. J. Strait, H. Takahashi, A. S. Welander, T. Bolzonella, R. V. Budny, J. S. Kim, R. Hatcher, Y. Q. Liu, and T. C. Luce, *Nucl. Fusion* **49**, 125003 (2009).
- ⁵Y. Liu, I. T. Chapman, M. S. Chu, H. Reimerdes, F. Villone, R. Albanese, G. Ambrosino, A. M. Garofalo, C. G. Gimblett, R. J. Hastie, T. C. Hender, G. L. Jackson, R. J. La Haye, M. Okabayashi, A. Pironi, A. Portone, G. Rubinacci, and E. J. Strait, *Phys. Plasmas* **16**, 056113 (2009).
- ⁶S. A. Sabbagh, J. W. Berkery, R. E. Bell, J. M. Bialek, S. P. Gerhardt, J. E. Menard, R. Betti, D. A. Gates, B. Hu, O. N. Katsuro-Hopkins, B. P. LeBlanc, F. M. Levinton, J. Manickam, K. Tritz, and H. Yuh, *Nucl. Fusion* **50**, 025020 (2010).
- ⁷S. A. Sabbagh, R. E. Bell, J. E. Menard, D. A. Gates, A. C. Sontag, J. M. Bialek, B. P. LeBlanc, F. M. Levinton, K. Tritz, and H. Yuh, *Phys. Rev. Lett.* **97**, 045004 (2006).
- ⁸P. R. Brunzell, D. Yadikin, D. Gregoratto, R. Paccagnella, T. Bolzonella, M. Cavinato, M. Cecconello, J. R. Drake, A. Luchetta, G. Manduchi, G. Marchiori, L. Marrelli, P. Martin, A. Masiello, F. Milani, S. Ortolani, G. Spizzo, and P. Zanca, *Phys. Rev. Lett.* **93**, 225001 (2004).
- ⁹R. Paccagnella, S. Ortolani, P. Zanca, A. Alfier, T. Bolzonella, L. Marrelli, M. E. Puiatti, G. Serianni, D. Terranova, M. Valisa, M. Agostini, L. Apolloni, F. Auriemma, F. Bonomo, A. Canton, L. Carraro, R. Cavazzana, M. Cavinato, P. Franz, E. Gazza, L. Grando, P. Innocente, R. Lorenzini, A. Luchetta, G. Manduchi, G. Marchiori, S. Martini, R. Pasqualotto, P. Piovesan, N. Pomaro, P. Scarin, G. Spizzo, M. Spolaore, C. Taliercio, N. Vianello, B. Zaniol, L. Zanutto, and M. Zuin, *Phys. Rev. Lett.* **97**, 075001 (2006).
- ¹⁰A. M. Garofalo, E. J. Strait, L. C. Johnson, R. J. La Haye, E. A. Lazarus, G. A. Navratil, M. Okabayashi, J. T. Scoville, T. S. Taylor, and A. D. Turnbull, *Phys. Rev. Lett.* **89**, 235001 (2002).
- ¹¹E. J. Strait, A. M. Garofalo, G. L. Jackson, M. Okabayashi, H. Reimerdes, M. S. Chu, R. Fitzpatrick, R. J. Groebner, Y. In, R. J. LaHaye, M. J. Lanctot, Y. Q. Liu, G. A. Navratil, W. M. Solomon, and H. Takahashi, *Phys. Plasmas* **14**, 056101 (2007).
- ¹²C. C. Hegna, *Phys. Plasmas* **11**, 4230 (2004).
- ¹³C. G. Gimblett, *Plasma Phys. Controlled Fusion* **31**, 2183 (1989).
- ¹⁴C. G. Gimblett and R. J. Hastie, *Phys. Plasmas* **7**, 5007 (2000).
- ¹⁵M. V. Umansky, R. Betti, and J. P. Freidberg, *Phys. Plasmas* **8**, 4427 (2001).
- ¹⁶M. Kruskal and M. Schwarzschild, *Proc. R. Soc. London, Ser. A* **223**, 348 (1954).
- ¹⁷V. Shafranov, *At. Energ.* **1**, 709 (1956).
- ¹⁸A. W. Hood, *Plasma Phys. Controlled Fusion* **34**, 411 (1992).
- ¹⁹W. F. Bergerson, C. B. Forest, G. Fiksel, D. A. Hannum, R. Kendrick, J. S. Sarff, and S. Stambler, *Phys. Rev. Lett.* **96**, 015004 (2006).
- ²⁰W. F. Bergerson, D. A. Hannum, C. C. Hegna, R. D. Kendrick, J. S. Sarff, and C. B. Forest, *Phys. Rev. Lett.* **101**, 235005 (2008).

- ²¹G. Fiksel, A. F. Almagri, D. Craig, M. Iida, S. C. Prager, and J. S. Sarff, *Plasma Sources Sci. Technol.* **5**, 78 (1996).
- ²²D. J. D. Hartog, D. J. Craig, G. Fiksel, and J. S. Sarff, *Plasma Sources Sci. Technol.* **6**, 492 (1997).
- ²³J. Wesson and J. W. Connor, *Tokamaks* (Clarendon, Oxford 1987).
- ²⁴M. D. Nornberg, E. J. Spence, R. D. Kendrick, C. M. Jacobson, and C. B. Forest, *Phys. Rev. Lett.* **97**, 044503 (2006).
- ²⁵G. Fiksel, D. J. D. Hartog, and P. W. Fontana, *Rev. Sci. Instrum.* **69**, 2024 (1998).
- ²⁶E. G. Zweibel and M. Yamada, *Annu. Rev. Astron. Astrophys.* **47**, 291 (2009).
- ²⁷I. Furno, T. P. Intrator, E. W. Hemsing, S. C. Hsu, S. Abbate, P. Ricci, and G. Lapenta, *Phys. Plasmas* **12**, 055702 (2005).
- ²⁸M. G. Linton, *Phys. Plasmas* **13**, 058301 (2006).